

Chapter 4: Making BECs in the Rubidium Lithium apparatus

All the experiments presented in this thesis were performed at the Rubidium-Lithium (RbLi) apparatus at the University of Maryland. The apparatus was designed to produce mixtures of quantum degenerate gases of bosons and fermions. The original plan was abandoned because the cross-species scattering length was found to be repulsive and small ($a_s \approx 20 a_B$) [57] and the nearest Feshbach resonance was measured to occur at the unexpectedly large magnetic field of 1066 G [58]. All our experiments were performed using only ^{87}Rb instead.

The RbLi apparatus is scheduled to be shut down and the construction of a new dual-species apparatus for ^{87}Rb and ^{39}K is underway. The RbLi apparatus has been thoroughly described in [37,38] so I only give a brief overview of the apparatus. I additionally discuss in detail the new elements that have been added to the setup and implemented changes not previously reported. In Appendix A I discuss the best and the worst aspects of the apparatus and in Appendix B I discuss some aspects of the construction of the new apparatus for those interested to look deeper into the technical aspects of experimental apparatus.

This Chapter is divided into three sections. In Section 4.1 I give a brief overview of the RbLi apparatus and describe its basic capabilities. In Section 4.2 I

describe the experimental sequence used to produce BECs. Finally in Section 4.3 I describe changes ~~and~~ to the RbLi apparatus that were not previously reported.

4.1 Overview of the RbLi apparatus

The RbLi apparatus is divided into two optical tables. One table contains laser systems that are fiber-coupled into the main experiment optical table, shown in Figure 2, containing a vacuum system where atoms are cooled to degeneracy. The vacuum system can be divided into three regions: an oven ~~Region~~ where Rb and Li atoms are heated up, a Zeeman slower that acts as a differential pumping stage and an ultra-high vacuum (UHV) region with a glass cell ~~where all the experiments are performed~~.

4.1.1 Laser systems

We use a ~~total~~ of three lasers to perform laser cooling and imaging of atoms: a cooling laser that addresses the $F = 2 \rightarrow F' = 3$ transition, a repump laser that takes atoms that have decayed into the $F = 1$ state back to $F = 2$ via the $F' = 1$ state and a master laser that provides a frequency reference for both lasers. The frequency of the master laser is locked using saturation absorption spectroscopy to the $F = 3 \rightarrow F' = 3$ and $F = 3 \rightarrow F' = 4$ crossover of the D2 line of ^{85}Rb . A fraction of repump and cooling light is used in beam for performing laser-cooling in the Zeeman slower and most of the remaining light is combined in six beams used to create a magneto-optical trap (MOT). We have two additional beams with cooling

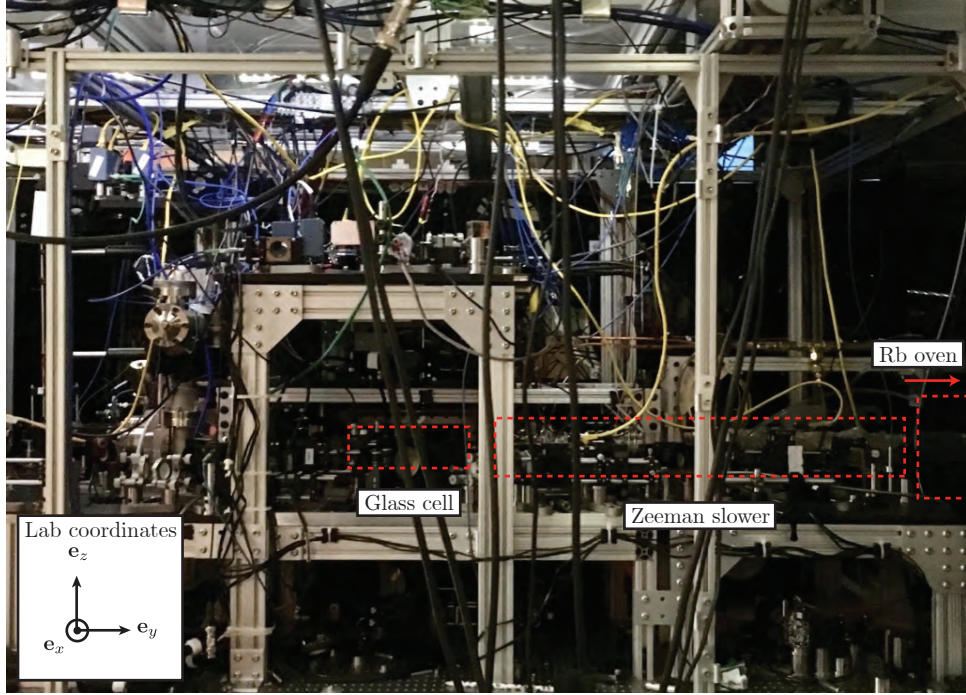


Figure 1: The vacuum system of the RbLi apparatus is divided into an oven, a Zeeman slower and an UHV region containing a glass-cell where all experiments are performed.

light used for imaging the atoms along two different directions. The frequencies of each laser with respect to the master laser frequency with respect to the transitions in ^{87}Rb can be visualized in Figure 2.

We have two additional lasers that are used to generate potentials for the atoms. The first one is a 30 W 1064 nm IPG Photonics laser located at the main experiment table and that we use to make a cross dipole trap for the atoms. The two dipole beams come from the zeroth and first order of an acousto-optic modulator (AOM) and the beams propagate along the $\mathbf{e}_x + \mathbf{e}_y$ and $\mathbf{e}_x - \mathbf{e}_y$ direction (the lab coordinate system is shown in Figure 2). The other laser system is a Ti:Sapphire laser used to generate Raman transitions and will be described in more detail in

Section 4.3.2.

We can detect atoms using two different imaging systems. The first one is used primarily for diagnostics and it images the yz plane of the atoms from the $+e_x$ side of the glass cell. The second system looks at the xy plane from below the glass cell and is the main system used for data acquisition. Figure 3 shows a simplified diagram with a top and a side view of the apparatus including all the lasers that are used for cooling, trapping, Raman coupling and imaging.

4.1.2 Magnetic field control

The precise control of magnetic fields is essential during the multiple stages in our experimental sequence. The RbLi apparatus has multiple coils as is illustrated in Figure 4. Three pairs of Helmholtz coil in the vicinity of the glass cell generate bias magnetic fields $\mathbf{B} = (B_x, B_y, B_z)$ along e_x , e_y and e_z . Once BECs are produced we typically use bias fields along e_z to change the Zeeman energy of the different $|m_F\rangle$ states. One pair of anti-Helmholtz coil generates a strong quadrupole magnetic field along e_z that is used in the MOT, for magnetic trapping, and to separate the different $|m_F\rangle$ states before imaging via the Stern-Gerlach effect. An additional set of coils arranged in a ‘cloverleaf’ pattern generates small gradients along e_z , $e_x + e_y$ and $e_z - e_y$ which allow us to cancel stray magnetic gradients in B_z near the atoms.

The experiment also has the capability of producing oscillatory magnetic fields. A set of coils on a printed circuit board (PCB) and placed right above the glass cell produce linearly polarized radio-frequency (RF) magnetic fields either in the e_y or e_z

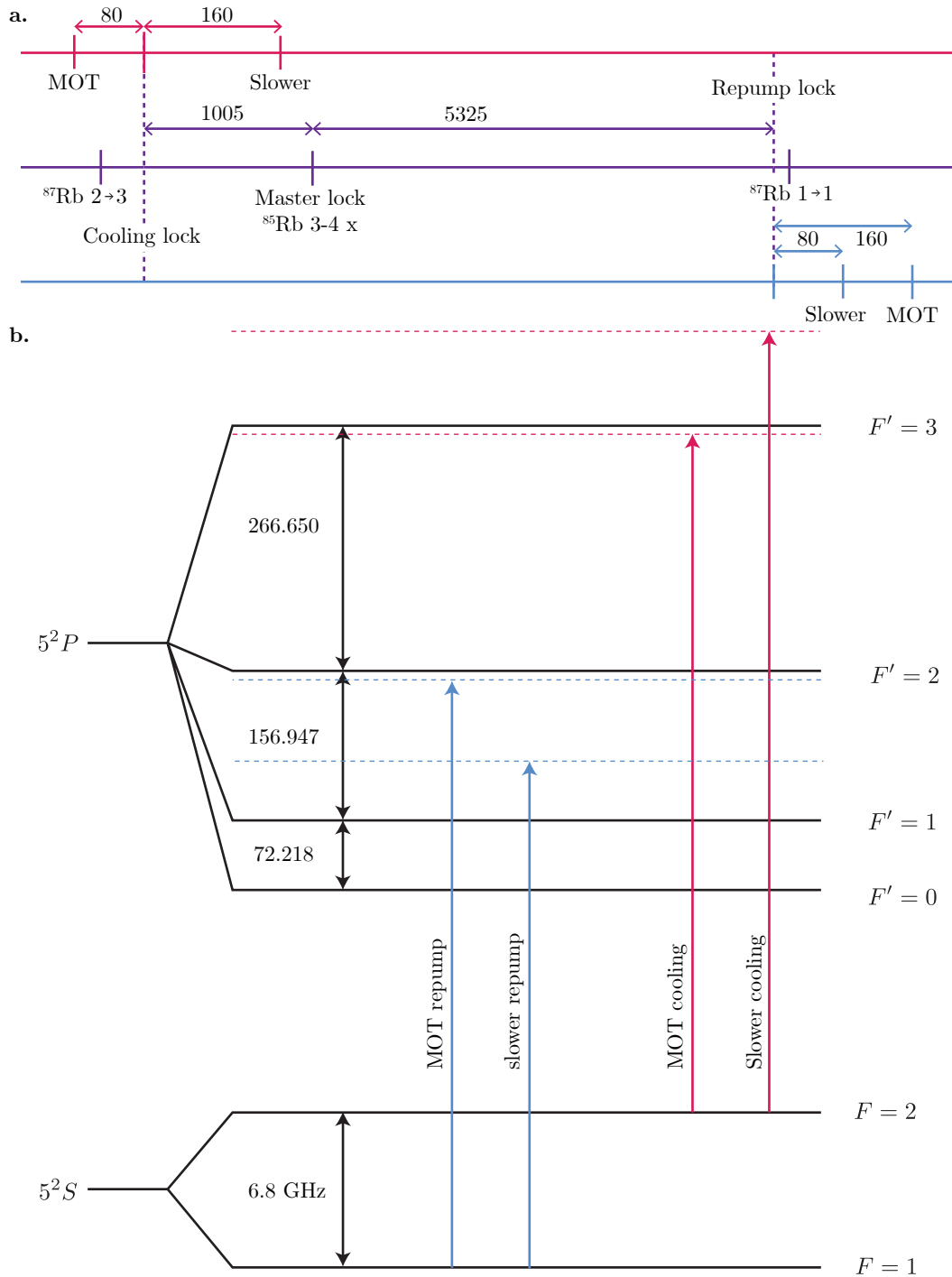


Figure 2: **a.** Cooling and repump frequencies relative to the master laser lock. **b.** Cooling and repump frequencies relative to the ^{87}Rb D2 line transitions.

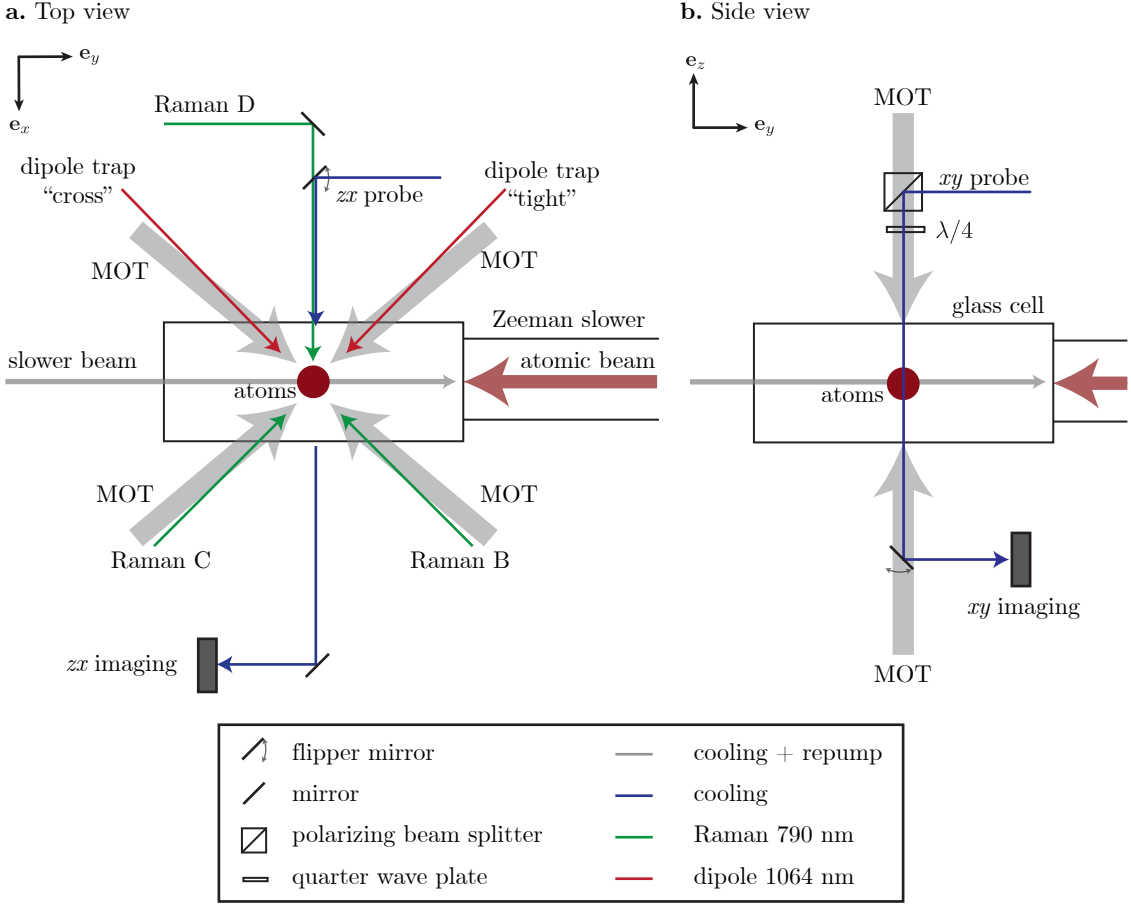


Figure 3: Diagram of the RbLi apparatus as seen from **a.** the top and **b.** the side.

direction that are used for RF induced evaporation and to drive transitions between $|m_F\rangle$ states. There is an additional setup for producing high-power RF fields which will be described in more detail in Section 4.3.3.

4.2 Experimental sequence to make BECs

The production of BECs starts in an oven where Rb atoms are heated to 120 C to produce an atomic beam. The Rb atoms come from the same 5 g ampule that was installed when the apparatus was first built almost 10 years ago. The atoms then

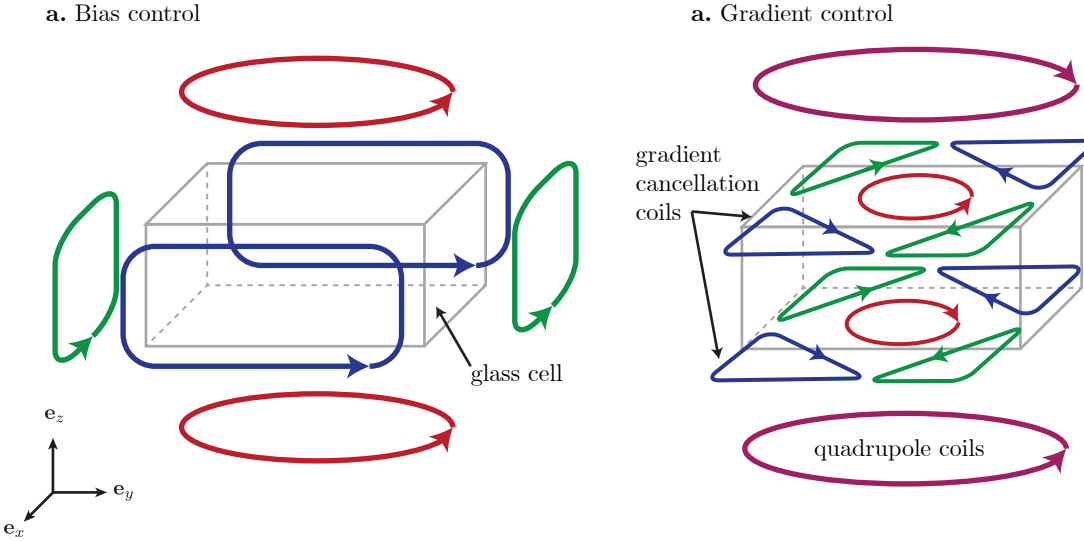


Figure 4: Magnetic coil geometry in the RbLi apparatus. **a.** We use three pairs of Helmholtz coils to produce bias fields along \mathbf{e}_x , \mathbf{e}_y and \mathbf{e}_z . **b.** We have a pair of coils that produce strong quadrupole magnetic fields for the MOT and magnetic trapping. Additionally we have a pair of ‘cloverleaf’ coils to control the gradients in B_z .

travel down a Zeeman slower [59] where they are laser cooled and then captured in a MOT. For the MOT we apply a 5.5 A current to the quadrupole coils corresponding to a 15.62 G/cm gradient. The cooling light is blue detuned by 18 MHz $\sim -3\Gamma$ from the $F = 2 \rightarrow F' = 3$ cycling transition and the repump light is 16 MHz below the $F = 1 \rightarrow F' = 2$ transition. We typically load the MOT for a total time of 1 – 5 s before we turn off the Zeeman slower currents. In preparation for the molasses stage we do a 30 ms decompression stage where we ramp down the gradient to 10 G/cm and reduce the repump power.

The atoms are cooled further down in an optical molasses stage due to the polarization gradient from interfering counter-propagating lasers [60]. For this stage we completely switch off the quadrupole coils and adjust the bias fields in all three di-

rections so that they are canceled at the atoms. During this stage, the repump power is kept low and the frequency of the cooling light is decreased to 140 MHz below the MOT frequency for 10 ms. We then completely turn off the MOT repump light allowing atoms to decay into the $F = 1$ manifold and use a small amount of repump light from the Zeeman slower to optically pump atoms into the $|F = 1, m_F = -1\rangle$ magnetically trappable state for a total of 1.5 ms.

Once the atoms are successfully pumped into $|F = 1, m_F = -1\rangle$ we capture them in a magnetic trap with a gradient of 62 G/cm and compress them by increasing the current in the coils until we reach a gradient of 160 G/cm in 300 ms to enhance the elastic collisional rates and promote faster thermalization during evaporation. We perform RF-induced evaporation in the magnetic trap by turning on an RF field polarized along \mathbf{e}_y with a frequency of 24 MHz, which transfers the hotter atoms at the edges of the trap into the $m_F = 0$ state which is not magnetically trappable. We then perform an exponential ramp from the initial frequency to a final frequency of 4.5 MHz in 1 s, and as the frequency is swept the most energetic atoms are selectively transferred into untrappable states.

For the final stage of evaporative cooling, we transfer the atoms from the magnetic trap into an optical dipole trap. We start by turning on only the ‘tight’ arm of the trap at full power (about 11 W) and slowly decompressing the quadrupole trap to 45 G/cm in 1.5 s. We then turn on the second ‘cross’ beam in 1 s, splitting the power so that 70 – 30% is distributed between the tight and cross beams. As the cross dipole beam is being turned on, we ramp the quadrupole field further down to 14 G/cm, slightly above the value necessary for the trap to suspend atoms against

gravity while simultaneously shifting the bias field along \mathbf{e}_z to align the center of the quadrupole trap to the dipole trap.

We evaporate atoms in the dipole trap in two stages. First we exponentially ramp down the power to about 20% of its initial power in 1.5 s (0.5 s $1/e$ time). Before the final evaporation stage we completely turn off the quadrupole trap in 1 s. Finally, we perform a second exponential ramp where the power is dropped to about 30% of the intermediate power in 2 s (1 s $1/e$ time). The slow ramps ensure that there is enough time for the atoms to thermalize as they evaporate. During the second evaporation stage the atoms reach the critical temperature for Bose-Einstein condensation and we are able to produce BECs with about 4×10^4 atoms in the $|F = 1, m_F = -1\rangle$ state. To transfer atoms into different $|F, m_F\rangle$ states within the ground $5^2S_{1/2}$ manifold we use the ARP protocol described in Section 3.5.2.

Our experiments are very sensitive to changes in the environmental magnetic field. In the past we used flux gate sensors (**Stefan-Mayer** model FL1-100 f) in the apparatus to feedback and stabilize the magnetic field (see [38]). These sensors are a useful tool, however due to space constraints we were not able to measure the fields close to the atoms and additionally the range of magnetic fields that they operate at is small (only 1 G, we typically operate at $B > 10$ G). We built a 6.8 GHz microwave system (see Section 4.3.4) so that we could use the atoms themselves as sensors of magnetic field. Once BEC is achieved and before performing any experiment, we typically use a protocol involving two microwave assisted partial transfer absorption images described in Section 3.5.3 to monitor and stabilize the magnetic field at the atoms.

To keep the bias magnetic fields as stable as possible we additionally synchronize the timing of our experiments to the 60 Hz line; this step is performed in different stages of the experiment but its biggest impact is right before performing any magnetically sensitive experiment.

4.3 Upgrades to the RbLi Machine

4.3.1 Master laser system

Previously we used a **New Focus Vortex II TLB-6900** extended cavity diode laser as our master laser locked using a homemade saturation spectroscopy setup using a Rb glass cell and an FPGA based PID circuit (see [37, 38]). The frequency of this laser was not very stable and the laser would constantly get out of lock. We replaced the old master laser with a **Vescent photonics DBR Laser Module System** which uses a distributed Bragg reflector laser diode with no external cavity and is therefore very mechanically stable. The frequency of the laser is stabilized and controlled using the D2-210 spectroscopy module and D2-125 laser servo. The master laser system is considerably simplified as can be seen in Figure 5 and the lab no longer suffers from an unstable master laser.

4.3.2 Raman laser system

The RbLi apparatus has a laser system with wavelength close to 790 nm that is used to generate Raman induced transitions and spin-dependent potentials (see Section 3.3.2). The original Raman laser system consisted of a **Toptica DL Pro**

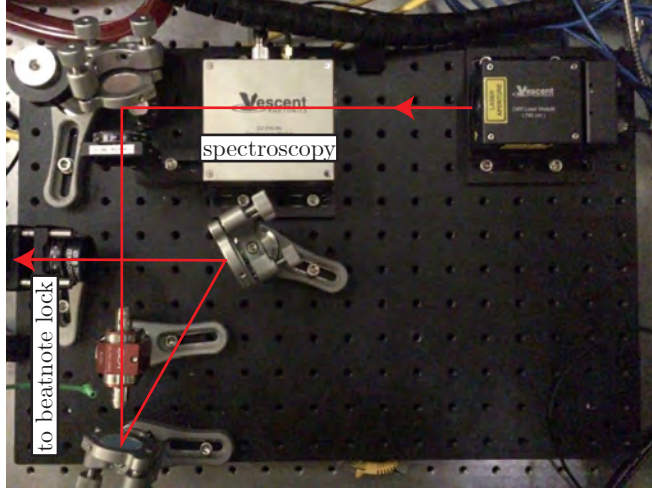


Figure 5: Master laser system. We replaced the old Vortex II laser with a Vescent photonics DBR Laser Module System that is considerably more stable.

laser seeding a tapered amplifier chip mounted on a homemade copper holder. This laser system was replaced by an M squared Ti:Sapphire laser (**SolsTiS-400-SRX-F**) that is pumped by a 532 nm **IPG GLR30** laser. We typically operate the pump laser at 14.5 W. A fraction of this light is redirected into the path of a 1D optical lattice and the remaining power is used to pump the Ti:Sahpire laser. Figure 6 shows the **typical** dependence of the Ti:Sapph output power as a function of pump power. We switched to using a Ti:Sapph laser because of its wide range of tunable wavelengths in the near infrared (725 – 875 nm) and its high power output. In addition to this, the TA system had considerable amplified spontaneous emission (ASE) close to 780 nm which caused increased scattering of photons and reduced lifetimes due to our inability to completely filter it.

The output of the laser is split into 3 different Raman beams. The frequency and power of each beam is independently controlled using **IntraAction ATM-801A2** AOMs centered at 80 MHz. We drive the AOMs using homemade drivers made from

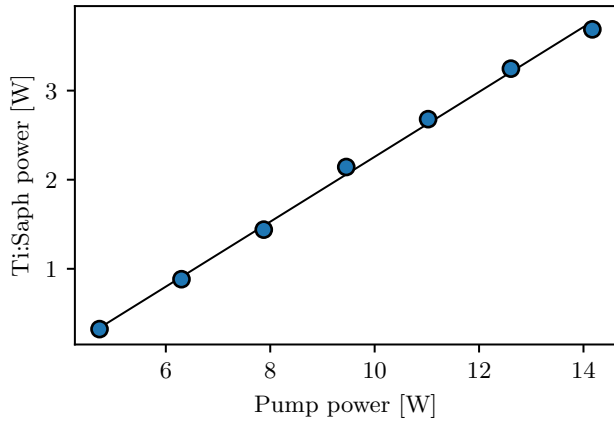


Figure 6: Ti:Sapphire laser output as a function of pump power. This data was taken when the laser was being setup for the first time. The alignment of the laser cavity was optimized to produce maximum power at 15 W pump power. The output power is proportional to the pump power $P_{\text{out}} \approx 0.364P_{\text{pump}}$.

the `Minicircuits` components listed in Table 4.1 and `Novatech Model 409B` direct digital synthesizer (DDS) to generate an RF signal at the desired frequency. ~~The components are arranged as is shown in Figure 8:~~ we control the amplitude of the RF signal using a mixer connected to a DC signal and the switch can turn off the signal in less than $1\ \mu\text{s}$ using a TTL signal. We fiber-couple the light using single-mode optical fibers (non-polarization maintaining) with angle-cut FC/APC type connectors at the input (laser side) and flat-cut FC/PC at the output (experiment side). We made this choice so to implement a phase lock that would cancel phase noise added by the fibers. The idea behind this method is that a small fraction of the fiber-coupled light is reflected at the flat-cut edge of the optical fiber and coupled back where it can be heterodyne probed with the input light (see Figure 7). Our implementation of the fiber phase lock is based on Section 3.6.3 of [61]. Because the fibers are not polarization maintaining we control the output polarization of

the light using paddles (Thorlabs FPC030 and Thorlabs FPC560) that produce a controllable amount of stress in the fibers and ~~therefore~~ changes their birefringence. This method makes injecting light into the fiber very straightforward and painless because, unlike with polarization-maintaining fibers, the polarization of the incoming light can be arbitrary and does not need to be aligned to any fiber axis. None of the experiments presented in this thesis used the phase lock but the experiments described in Chapter 8 were performed using the new Raman laser system. Figure 7 shows a diagram of the Raman optics as well as the 532 nm optical lattice optics which are shared on the same breadboard.

Table 4.1: List of AOM driver components

Part number	Description
ZHL-1-2W	2 W amplifier
ZAD-3+	Mixer
ZYSWA-2-50DR	Digital switch

4.3.3 High power RF system

The experiments described in Chapters 6 and 8 required the use of high power RF magnetic fields to achieve coupling strengths at the atoms $\Omega \sim 100 - 200$ kHz. After multiple attempts to build a resonant coil either on a PCB (similar to the coil used for RF induced evaporation, see [37, 38]) or winding some wires with the right dimensions we found that the product that worked best for our needs was a wireless power charging receiver coil (Würth Elektronik Digikey part number 732-5646-ND) shown in the bottom panel of Figure 4.3.3a. The coil has a self-

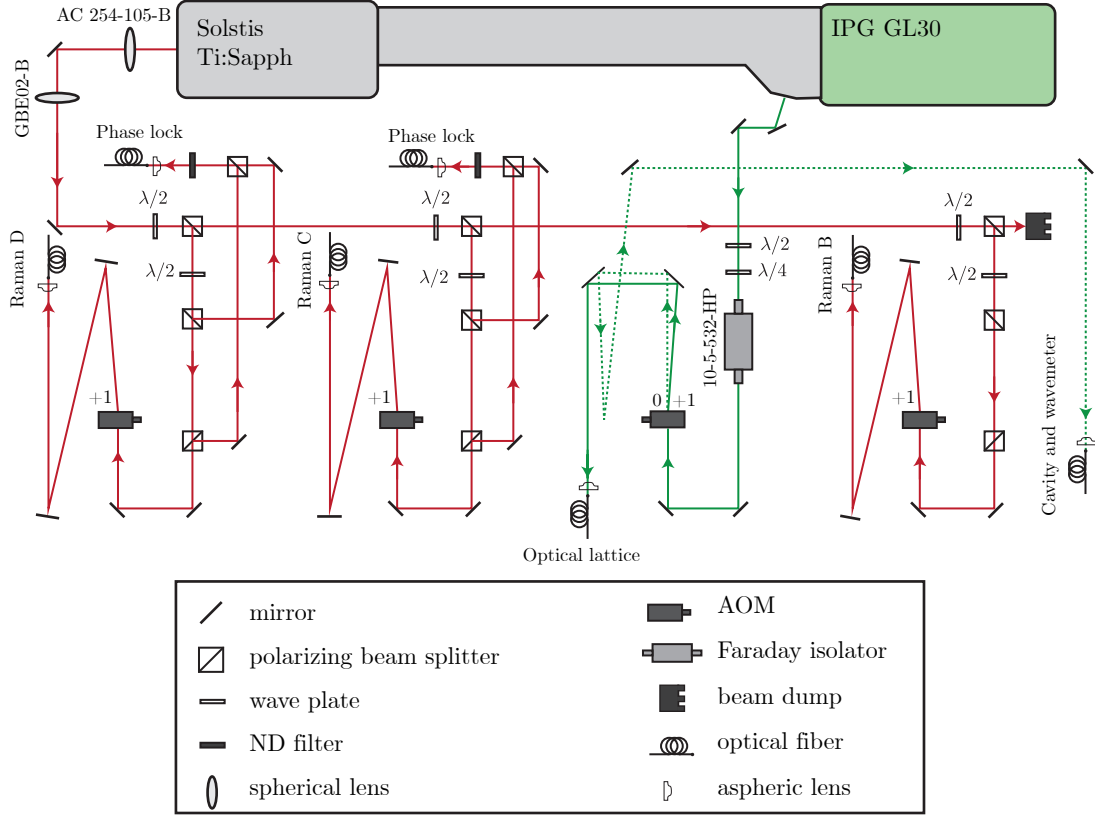


Figure 7: Optical layout of Raman and optical lattice lasers. The Ti:Sapphire laser provides tunable infrared light that we use for three different Raman beams. The beams labeled as ‘Raman C’ and ‘Raman D’ can be phase stabilized. A small fraction of the green pump laser is used to produce a blue-detuned 1D optical lattice.

resonant frequency at 22 MHz and a Q-Factor of 45. It has an inner diameter of 1.62 cm and an outer diameter of 2.8 cm, just the right size for us to place it snugly next to the glass cell (on the $-e_x$ side) with minimal perturbations to the laser beams in its vicinity (it only slightly clips one MOT beam).

The loop is mounted on the PCB shown in Figure 9. The board has two connections: the top one in Figure 9 has a small loop used as a pickup antenna that we attach to a power detector **Minicircuits ZX47-40-S+** to monitor the power and the bottom lines have pads that can be used to make an impedance matching

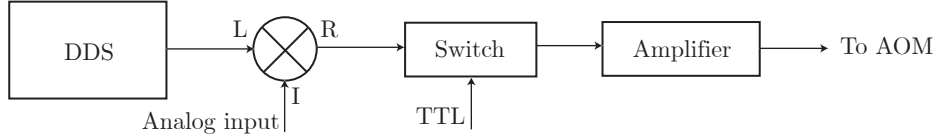


Figure 8: Setup used to drive the AOMs controlling the power and frequency of Raman beams. A similar setup is used to drive a coil used to generate high-power RF fields at the atoms.

network.

We used a vector network analyzer (VNA) to ~~help us~~ perform the impedance matching. The VNA sends a small amplitude frequency into the circuit and measures the amplitude and phase of the reflected power from which the impedance can be inferred. Figure 10a shows the reflected power as a function of frequency for a test circuit and Figure 10b shows the complex valued impedance as a function of frequency displayed on a Smith chart. The Smith chart is a helpful way to visualize the impedance of a circuit: the black circles correspond to constant resistance, with the rightmost point corresponding to an open circuit (infinite resistance) and the largest circle corresponding to a short circuit (zero resistance). The arcs correspond to constant reactance; the horizontal axis corresponds to zero reactance ($\text{Im}(Z) = 0$), the top arcs correspond to $\text{Im}(Z) > 0$, and the lower arcs to $\text{Im}(Z) < 0$. The circuit is impedance matched when $Z = 50 \text{ Ohm}$ (the center of the Smith chart), the standard value of RF transmission lines. We tested different components on the pads until we found a peak in reduced reflected power at the desired frequency. It is also important to note that it was essential that the circuit was installed in its final location in the experiment when measuring the impedance as the other parts

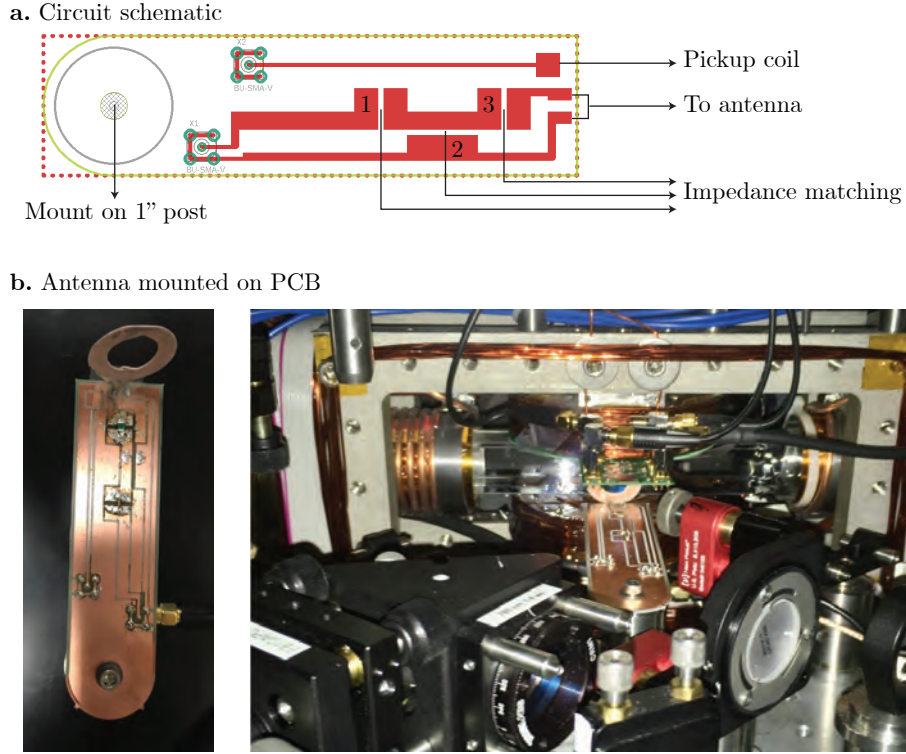


Figure 9: We use a commercial resonator with an impedance matching network to produce high power RF fields. **a.** Diagram of the impedance matching network. **b.** A picture of the resonator mounted on a PCB. We place this device as close to the atoms as possible next to the glass cell.

in the vicinity of the antenna can shift the resonant frequency.

The driving electronics are very similar to the AOM drivers described in Section 4.3.2. The only difference is we use a 30 W amplifier ([Minicircuits LZY-22+](#)) instead of the smaller amplifiers needed to drive the AOMs.

4.3.4 6.8 GHz microwave system

We built a 6.8 GHz microwave system to couple atoms between the $F = 1$ and $F = 2$ ground hyperfine manifolds of ^{87}Rb . We mostly use this system to stabilize the bias magnetic field along \mathbf{e}_z at the atoms using microwave assisted PTAI

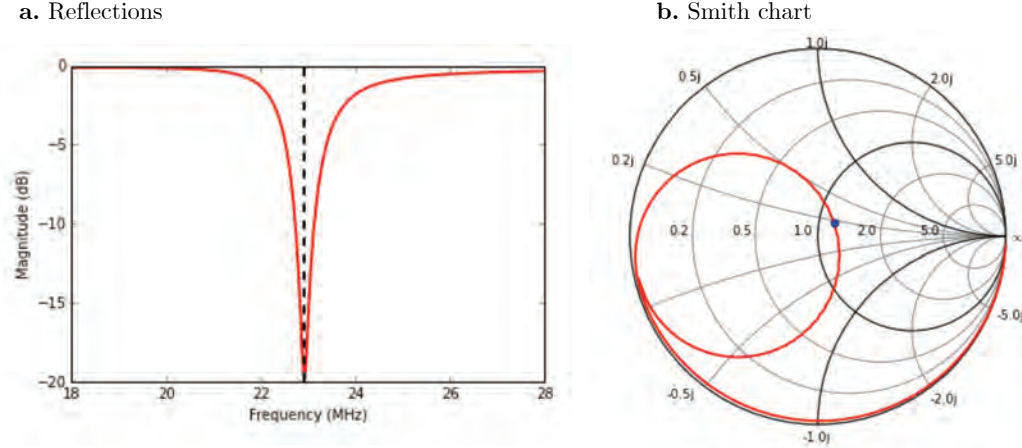


Figure 10: Impedance matching of high power RF antenna. **a.** Reflected power as a function of frequency. **b.** Impedance as a function of frequency, visualized on a Smith chart.

(Section 3.5.3). A list of components used in the setup is presented in Table 4.2 and a diagram of the connections is displayed in Figure 11.

Table 4.2: 6.8 GHz microwave system components

Part number	Description
SRS SG384	Signal generator
Narda 4014C-30	Directional coupler
Marki IRW0618	Mixer
Minicircuits VBFZ-6260-S+	Bandpass filter 6 – 8 GHz
Herley D1956	Voltage controlled attenuator
MSI MSH-5727901	46 dB gain amplifier
Narda 4014C-30	Circulator
Minicircuits ZX47-40-S+	Power detector
Maury microwave 1819C	Stub tuner
ZYSWA-2-50DR	Digital switch

The SRS generator serves as a source of a fixed frequency and amplitude signal. We control the frequency by mixing a programmable ~ 100 MHz signal from a Novatech into a double balanced mixer; the RF signal can be turned on or off

using a TTL switch. The amplitude is controlled by commanding $0\text{--}6$ V signal from the control computer into an attenuator. The signal is amplified by +43 dB using an amplifier mounted on a water cooled plate. The microwave signal is broadcast to the atoms using a horn antenna. In order to get a coupling microwave coupling strength of the order of 10 kHz or larger it was important to place the horn as close to the atoms as possible and impedance matching the transmission line to maximize the radiated power. We additionally use a circulator that prevents any reflected power to go back into the amplifier and couplers at different locations to monitor the performance of the system. The last coupler and the circulator of the system are connected to a power detector that outputs a DC signal proportional to the microwave power. The impedance is tuned with a stub tuner by changing the length of the stubs until the reflected power measured at the exit port of the circulator is minimized at the desired frequency of operation.

4.4 Computer control and data acquisition

There have been two main changes in our computer control and data acquisition system. We have transitioned from using a LabVIEW based control system to a Python based control system, The `labscript suite` [62]. With the previous control software the lab devices were programmed using a graphic interface. `Labscript` instead uses a hybrid approach in which the experimental sequences are text based scripts. The use of scripted programming has given us more flexibility and modularity for programming experiments and additionally, it is now very easy

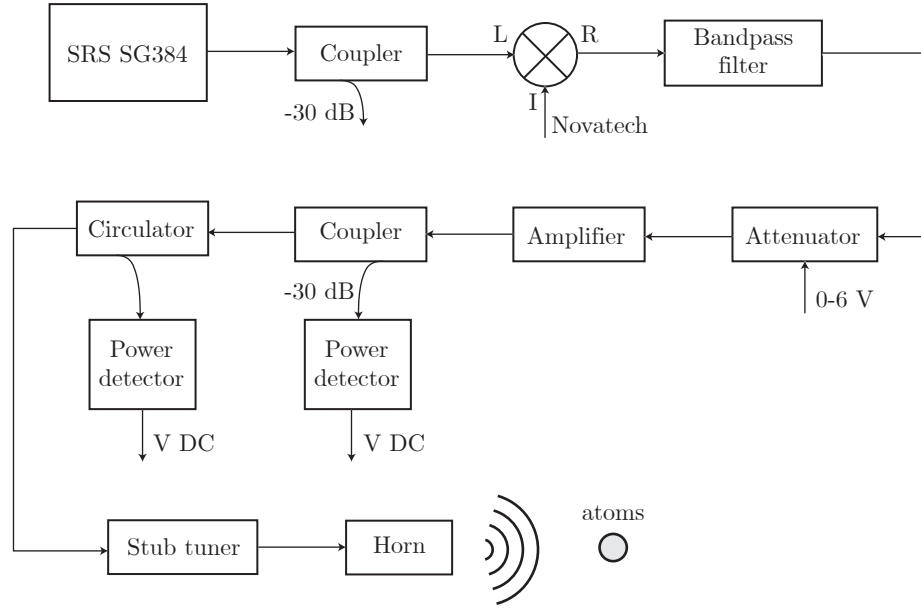


Figure 11: Schematic of 6.8 GHz microwave system.

to do multi-dimensional parameter scans. Each experimental shot is saved in a Hierarchical Data Format version 5 file (HDF5) that includes images from cameras, oscilloscope traces, and analog inputs as well as copy of the script used in the experiment and the values of all of the parameters used. This has been a great upgrade as we no longer rely on the person running an experimental sequence pushing the ‘save’ button and thoroughly documenting the experiment in question¹.

The other upgrade worth mentioning is replacing our old **Flea3** (FL3-FW-03S1M-C from **FLIR**, formerly **Point Grey**) CCD camera with a **Mako G-030** camera from **Allied Vision**. With this new camera the time between two consecutive shots can be as short as $96\ \mu\text{s}$ (we used to wait $\sim 30\ \text{ms}$ with the Flea3 camera), greatly reducing the effect of mechanical vibrations in the experiment that produce fringes in the

¹As I have been digging into old data, I greatly wish we had this feature sooner.

absorption images. Table 4.3 summarizes relevant specifications of both cameras.

In our experimental sequence the probe and atoms images are separated by $150 \mu\text{s}$, which is not enough time for the atoms in the first absorption image to be cleared out. We therefore had to change the order in the absorption imaging protocol: first we take a picture of the probe which is 6.8 GHz detuned and minimally disturbs the atoms, we then apply repump light during the $150 \mu\text{s}$ interval in between the images to transfer atoms into $F = 2$ and then take the absorption image of the atoms. Figure 12 shows the OD computed using both cameras with no atoms present. When there is a long interval in between the two images the probe captured on the camera changes, leading to the fringes shown in Figure 12a. In contrast for probe images captured within a short interval the main noise contribution is shot noise as can be seen in Figure 12b. The addition of this camera was essential to get a better signal to noise ratio in the experiments reported in Chapter 8.

Table 4.3: Relevant specifications of Flea3 and Mako cameras.

	Flea3	Mako
Sensor type	CCD	CMOS
Quantum efficiency at 780 nm	$\sim 40\%$	$\sim 30\%$
Dark noise	19.94 e/s	12.9 e/s
Frame rate at max resolution	120 fps	309 fps
Pixel size	$5.6 \times 5.6 \mu\text{m}$	$7.4 \times 7.4 \mu\text{m}$
Resolution	648×488	644×484
Dynamic range	65 dB	56.7 dB
Analog to digital converter	12 Bit	12 Bit

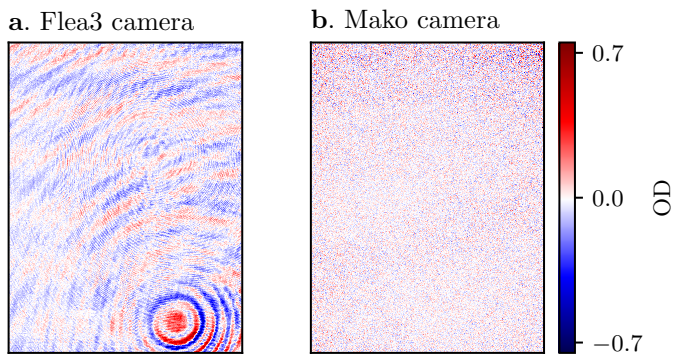


Figure 12: OD computed using two consecutive probe images without atoms. **a.** With the Flea3 camera images are spaced by ~ 30 ms. Changes in the probe result in fringes in the OD. **b.** With the Mako camera images are spaced by $\sim 150 \mu\text{s}$. ~~The main source of noise in the OD is shot noise.~~